Constraints on the End of Reionization from the Density Fields Surrounding Two Highly Opaque Quasar Sightlines

Holly M. Christenson[1] , George D. Becker[1] , Steven R. Furlanetto[2] , Frederick B. Davies[3] , Matthew A. Malkan[2] ,
Yongda Zhu[1] , Elisa Boera[4], and Adam Trapp[2]

[1] Department of Physics and Astronomy, University of California, Riverside, CA 92521, USA; hchri004@ucr.edu
[2] Department of Physics and Astronomy, University of California, Los Angeles, CA 90095, USA
[3] Max Planck Institut für Astronomie, Heidelberg, Germany
[4] INAF Osservatorio Astronomico di Trieste, Trieste, Italy

Abstract

The observed large-scale scatter in Lyα opacity of the intergalactic medium at $z < 6$ implies large fluctuations in the neutral hydrogen fraction that are unexpected long after reionization has ended. A number of models have emerged to explain these fluctuations that make testable predictions for the relationship between Lyα opacity and density. We present selections of $z = 5.7$ Lyα-emitting galaxies (LAEs) in the fields surrounding two highly opaque quasar sightlines with long Lyα troughs. The fields lie toward the $z = 6.0$ quasar ULAS J0148+0600, for which we reanalyze previously published results using improved photometric selection, and toward the $z = 6.15$ quasar SDSS J1250+3130, for which results are presented here for the first time. In both fields, we report a deficit of LAEs within 20 h^{-1} Mpc of the quasar. The association of highly opaque sightlines with galaxy underdensities in these two fields is consistent with models in which the scatter in Lyα opacity is driven by large-scale fluctuations in the ionizing UV background or by an ultra-late reionization that has not yet concluded at $z = 5.7$.

Unified Astronomy Thesaurus concepts: Intergalactic medium (813); Reionization (1383); High-redshift galaxies (734); Lyman-alpha galaxies (978)

1. Introduction

Cosmic reionization was the last major phase transition in the history of the universe, during which radiation from the first luminous sources ionized neutral hydrogen in the intergalactic medium (IGM) and transitioned the universe from a mostly neutral to a highly ionized state (see Wise 2019 for a review). The physical properties of the IGM at reionization redshifts can be used to constrain the timing, duration, and sources of reionization, which have major implications on our understanding of the first luminous sources in the universe and their environments.

A number of observations now suggest that much of the IGM was reionized from $z \sim 6$–8. Measurements of the cosmic microwave background are consistent with an instantaneous reionization occurring at $z \sim 7.7 \pm 0.7$ (Planck Collaboration et al. 2020). Evolution in the fraction of UV-selected galaxies that show Lyα in emission suggests that significant portions of the universe remain neutral at $z \sim 7$–8 (Mason et al. 2018; Jung et al. 2020; Morales et al. 2021; and references therein). The presence of damping wings in $z \gtrsim 7$ quasar spectra (Mortlock et al. 2011; Greig et al. 2017, 2019; Bañados et al. 2018; Davies et al. 2018b; Wang et al. 2020) also suggests a largely neutral IGM at those redshifts. Meanwhile, the onset of Lyα transmission in quasar spectra suggests that reionization was largely complete by $z \sim 6$ (Fan et al. 2006; McGreer et al. 2011, 2015).

Recent studies, however, have suggested that signs of reionization may persist in the IGM considerably later than $z = 6$. Measurements of the Lyα forest toward high-redshift QSOs show a large scatter in the opacity of the IGM to Lyα photons at redshifts $\leqslant 6.0$ (Fan et al. 2006; Becker et al. 2015; Bosman et al. 2018, 2021; Eilers et al. 2018; Yang et al. 2020), which is unexpected long after reionization has ended. The observed scatter on 50 comoving h^{-1} Mpc scales has been shown to be inconsistent with simple models of the IGM that use a uniform ultraviolet background (UVB; Becker et al. 2015; Bosman et al. 2018, 2021; Eilers et al. 2018; Yang et al. 2020). The most striking example of this scatter is the large Gunn–Peterson trough associated with the $z = 6.0$ quasar ULAS J0148+0600 (hereafter J0148), which spans 110 h^{-1} Mpc and is centered at $z = 5.7$ (Becker et al. 2015). While some scatter in Lyα opacity is expected due to variations in the density field (e.g., Lidz et al. 2006), the extreme opacity in the J0148 field cannot be explained by variations in the density field alone. Several types of models have therefore emerged to explain the observed scatter as due to variations in the IGM temperature and/or ionizing background, or potentially the presence of large neutral islands persisting below redshift six.

One type of model is based on a fluctuating ultraviolet background, in which large-scale fluctuations in the photoionizing background drive the large-scale fluctuations in Lyα opacity. Galaxy-driven UVB models, in which the fluctuations in the ionizing background result from clustered sources and a short, spatially variable mean free path, have been considered by Davies & Furlanetto (2016), D'Aloisio et al. (2018), and Nasir & D'Aloisio (2020). In this scenario, highly opaque regions are associated with low-density voids that contain few sources and therefore have a suppressed ionizing background. Low-opacity regions, in contrast, would have a strong ionizing background from the association with an overdensity of galaxies. Alternatively, Chardin et al. (2015, 2017) proposed a model in which the ionizing background is dominated by rare, bright sources such as quasars, which naturally produces spatial fluctuations in the UVB. Because quasars are rare, bright sources, the resulting UVB is not tightly coupled to the density field. In this scenario, a trough is associated with a suppressed ionizing background due to a lack of nearby quasars. The quasar-driven model, however, is somewhat disfavored because the required number density of quasars is at the upper limit of observational constraints and may also be in
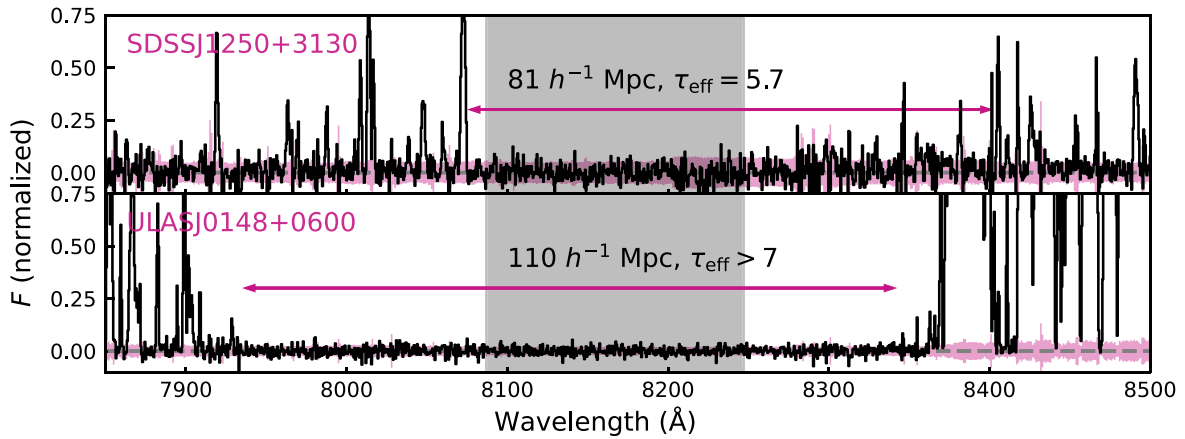
Figure 1. Partial spectra of the two quasars whose fields we observe with the Subaru/HSC. The top panel shows a Keck/ESI spectrum of SDSS J1250+3130, which exhibits a Lyα trough that is 81 h^{-1} Mpc in length with $\tau_{eff} = 5.7 \pm 0.4$ (Zhu et al. 2021). The bottom panel shows an X-Shooter spectrum of ULAS J0148+0600, which exhibits a 110 h^{-1} Mpc Lyα trough with $\tau_{eff} \geqslant 7$ (Becker et al. 2015). The approximate extent of each trough is indicated by the pink arrows. These quasars represent some of the most extreme Lyα troughs known at $z < 6$. The shaded gray region shows wavelengths covered by the NB816 filter with at least 10% transmittance, which corresponds to Lyα at $z \simeq 5.7$. The shaded pink region indicates the $\pm 1\sigma$ uncertainty interval.

conflict with observational constraints on helium reionization (D'Aloisio et al. 2017; McGreer et al. 2018; Garaldi et al. 2019).

D'Aloisio et al. (2015) proposed a model in which the opacity fluctuations are driven by large spatial variations in temperature, leftover from a patchy reionization process. In this scenario, overdense regions were among the first to reionize, and therefore have had more time to cool than less dense, more recently reionized regions. Absorption troughs such as the one toward J0148 are associated with overdense regions in this scenario; conversely, highly transmissive regions would be underdense.

More recently, a new type of model has emerged that suggests reionization may have ended later than $z \sim 6$, as widely assumed (Kulkarni et al. 2019a; Keating et al. 2020a, 2020b; Nasir & D'Aloisio 2020; Choudhury et al. 2021; Qin et al. 2021). In this scenario, the observed scatter in Lyα opacity is driven at least partly by islands of neutral hydrogen remaining in the IGM past $z = 6$. Troughs like the one associated with J0148, therefore, trace regions of the IGM that have not yet been reionized. The last places to become ionized in this model are low density, but those same underdense regions may quickly become highly transmissive once they have been reionized (Keating et al. 2020b). These models predict that both high- and low-opacity sightlines may be underdense (although see Nasir & D'Aloisio 2020, who find a large range in densities for transmissive lines of sight). We note that ultra-late reionization models typically also include a fluctuating UVB, but their defining feature is the presence of neutral islands at $z < 6$.

A key result of the attempts to model large-scale fluctuations in Lyα opacity is that each type of model makes strong predictions for the relationship between opacity and density, particularly for extremely high and low opacities. Both of these quantities can readily be measured; the opacity of a sightline can be obtained from a background quasar's Lyα forest, and a galaxy survey can be used to trace the underlying density. Davies et al. (2018a) demonstrated that surveys of Lyα emitters (LAEs) should be able to distinguish between these models for extremely high- and low-opacity sightlines. LAEs are a good choice for this type of observation because LAE surveys at $z \sim 6$ can be conducted with only three bands of photometry. Narrowband filters tuned to the atmospheric window near 8200 Å, corresponding to Lyα at $z = 5.7$, are also well matched to a redshift where large opacity fluctuations are present.

The results of a LAE survey in the J0148 field were published in Becker et al. (2018). These results were consistent with fluctuating UVB and late reionization models, and strongly disfavored the fluctuating temperature model. Kashino et al. (2020) followed up with a selection of Lyman break galaxies in the same field as a separate probe of density, and also reported a strong underdensity associated with the trough.

In this paper, we extend the study of the Lyα opacity-density relation to a second field surrounding a highly opaque quasar sightline. We provide an updated selection of LAEs toward ULAS J0148+0600, and present new results for SDSS J1250+3130, whose spectrum exhibits an 81 comoving h^{-1} Mpc Lyα trough. The LAE selections are based on updated LAE selection criteria, which we verify with spectroscopic follow-up of J0148 LAEs with Keck/DEIMOS. We summarize the observations in Section 2, and describe the photometry and LAE selection criteria in Section 3. The accompanying spectroscopy is presented in Appendix B. We present the results of LAE selections in both fields in Section 4, and compare the results to current reionization models in Section 5 before summarizing in Section 6. Throughout this work, we assume a ΛCDM cosmology with $\Omega_m = 0.3$, $\Omega_\Lambda = 0.7$, and $\Omega_b = 0.048$. All distances are given in comoving units, and all magnitudes are in the AB system.

2. Observations

Imaging data taken with the Subaru Hyper Suprime-Cam (HSC) were previously presented for the ULAS J0148+0600 field by Becker et al. (2018). The spectrum of ULAS J0148+0600 contains a 110 h^{-1} Mpc trough that has an effective optical depth of $\tau_{eff} \geqslant 7$, where $\tau_{eff} = -\ln \langle F \rangle$ and F is the mean continuum-normalized flux. For this work, we obtained HSC imaging of a second field, toward the $z = 6.15$ quasar SDSS J1250+3130 (hereafter J1250). The Lyα forest in the spectrum of J1250 contains a trough spanning 81 h^{-1} Mpc with $\tau_{eff} = 5.7 \pm 0.4$ (Zhu et al. 2021). The J1250 and J0148 fields represent some of the most highly opaque sightlines known at these redshifts. Figure 1 shows subsets of the X-Shooter spectrum for ULAS J0148+0600 (Becker et al. 2015) and the Keck/ESI spectrum for SDSS J1250+3130, displaying their Lyα troughs.

Table 1
Summary of HSC Imaging

	Filter	t_{exp} (hr)	Seeing[b]	$m_{5\sigma,\mathrm{PSF}}$[c]	$m_{5\sigma,1''.5}$[c]
J0148	r2	1.5	0.76	26.4	26.0
	i2	2.4	0.80	26.0	25.6
	NB816	4.5	0.73	25.2	25.0
J1250	r2	2.0[a]	0.83	26.4	26.2
	i2	2.5	0.81	26.1	25.8
	NB816	2.8	0.74	25.3	25.0

Notes.
[a] Partially observed in gray time.
[b] Median seeing FWHM in combined mosaic.
[c] Magnitude at which 50% of detected sources have S/N $\geqslant$ 5.

The J1250 field was observed via the HSC queue in 2019 April and June, with the majority of the data being taken during the dark time in April. Additional observations were taken during the dark time in 2020 May and 2021 January. As for the J0148 field, we obtained imaging centered on the quasar position in the NB816 filter, which has a mean transmission-averaged wavelength $\lambda = 8177$ Å, corresponding to Lyα emission at $z = 5.728$, and two broadband filters, i2 and r2. The narrowband observations were completed as planned, but the initial r2 observations in the J1250 field were completed in gray time and supplemented by additional dark time observations in 2020 May. We summarize the observations in both fields in Table 1.

We reduced the raw data with the LSST Science Pipeline, Versions 19 (J0148 field) and 21 (J1250 field; Jurić et al. 2015; Ivezić et al. 2019). The pipeline combines individual CCDs into stacked mosaics, using PanStarrs DR1 imaging (Chambers et al. 2016) for astrometric and photometric calibrations. We use Source Extractor (Bertin & Arnouts 1996) to identify the spatial coordinates of sources in the final stacked mosaics, and then make photometric measurements at those positions based on point-spread function (PSF) fitting, which we describe in more detail in Section 3.

Table 1 shows the median 5σ limiting PSF and aperture magnitudes in each band for both fields. These values represent the magnitudes at which at least 50% of the detected sources are measured at signal-to-noise ratios S/Ns $\geqslant$ 5.

We also use the imaging data to independently measure the Lyα opacity over the NB816 wavelengths along each quasar line of sight. The results are presented in Appendix A.

3. Methods

In this section we describe in detail the methods used to make photometric measurements and select LAE candidates.

3.1. Photometry

Becker et al. (2018) used CModel fluxes generated by the LSST pipeline, which are a composite of the best-fit exponential and de Vaucouleurs profiles (Abazajian et al. 2004; Bosch et al. 2018). We verified the quality of the flux calibration by checking the fluxes of 25 objects in each field from the SDSS catalogs. While the flux measurements for the verification objects were accurate to within the photometric errors, fluxes for faint, typically seeing-limited objects were found to be less reliable. For some of these objects, the best-fit CModel profile resulted in conspicuously high fluxes that were not in agreement with the fixed-aperture and PSF fluxes. This

systematic overestimation of CModel fluxes compromised the initial selection of LAEs in the J0148 field in two ways: objects that are not credible LAEs were selected as LAEs based on artificially high narrowband flux, and objects that could be credible LAEs were rejected based on artificially high broadband fluxes that resulted in failure of one or more color criteria. Examples of both types are shown in Appendix C.

To address these problems with the CModel fluxes, we implemented PSF measurements to replace the CModel measurements as the primary flux used in the analysis. The PSF photometry is optimized to maximize the detection of faint, often unresolved sources for the purpose of constructing a density map. Sources whose profiles are not well-represented by a PSF profile, such as extended sources, are assigned an aperture flux as their primary flux measurement, which we describe in more detail below. The photometry has the following steps:

1. At each source position identified and measured by Source Extractor in the combined mosaics, we measure the flux in a $''.15$ aperture.
2. We then measure the median sky background measured in a $5''$ annulus around the aperture, excluding any pixels that are flagged by the data reduction pipeline as sources.
3. A 2D Gaussian profile is fit over a stamp of the combined mosaic $10'' \times 10''$ in size centered on the source, using the measured sky background as the offset and holding the FWHM fixed to the median seeing. The only parameter allowed to vary is the amplitude.
4. Each pixel in the stamp is compared to the resulting fit. Pixels that differ from the model by more than five times the noise in the sky background are excluded from the next iteration of fitting. The primary purpose of this step is to reject cosmic rays and bad pixels.
5. The 2D Gaussian is fit again, excluding outlier pixels. After refitting, all pixels are again compared to the model and the exclusion, and the refitting process is repeated. Pixels that were previously rejected may be included in the next iteration of the fit. If the fitting exceeds ten iterations, more than 5% of pixels in the stamp are rejected, or more than 5% of the pixels within a $''.15$ aperture are rejected, the fit is considered a failure and the aperture flux is used as the primary flux measurement for that object. Typically, extended sources and other objects whose profiles are not well represented by the PSF profile will therefore be assigned aperture fluxes. If refitting fails to improve the fit (the same set of pixels are selected for exclusion in two subsequent iterations) but the maximum number of iterations and excluded pixels are not exceeded, the fit is considered a success and the resulting PSF flux is recorded. Approximately 20% of all sources fail, and 50% are refit at least once, most undergoing two iterations.

This PSF measurement is conducted for each band, independently of the others. We have allowed the fitting routine to default to aperture fluxes, because for many credible LAEs, the r2 and i2 fluxes are formally undetected, and the results of fitting a Gaussian to a field dominated by noise may be unpredictable. In these cases, we default to the aperture flux rather than accept a potentially bad fit.

3.2. LAE Selection Procedure

In addition to improving our photometric measurements, we have adjusted the criteria we use for selecting LAE candidates. Our observations in the J1250 field were made over the course

of three years, and the partially complete observations had large variations in depth across the three bands. This disparity motivated an adjustment of the selection criteria to account for the depth in each band. Our completed observations are still slightly uneven in depth across the three filters, and there are variations in depth between fields—for example, the J1250 field is slightly deeper than the J0148 field in both broadband filters. The revised selection criteria described do not dramatically change the LAE selection in these two fields; however, they reduce the number of selected objects by $\sim 25\%$. We emphasize that all sources must still pass a visual inspection to be accepted as LAE candidates.

The criteria originally used to select LAEs in the J0148 field were based on those used in Ouchi et al. (2008): $NB816 \leqslant 26.0$, $S/N_{NB816} \geqslant 5$, $i2 - NB816 \geqslant 1.2$, and $r2 \leqslant 2\sigma_{r2}$ or $r2 \geqslant 2\sigma_{r2}$ and $r2 - i2 \geqslant 1.0$. These requirements are designed to select line emitters and rule out low-redshift objects, but have no requirement for uncertainty or S/N in any band except the narrow band.

In order to account for the different depths of our photometric bands, we reexpress the selection criteria in terms of probability densities. For each color cut, we require that at least 50% of the probability density for that color is above the minimum acceptable color. We also require that 95% of the probability density be greater than the 1σ lower limit for an object with $S/N_{NB} = 5$ and $i2 - NB816 = 1.2$. The second requirement is designed to exclude objects that meet the minimum $i2 - NB816$ requirement but with large uncertainties.

Calculating the probability density for the color of each object is complicated somewhat by fluxes that are formally undetected. To calculate a physically motivated uncertainty for a color that is based on a non-detected flux (which may be negative), we used a set of artificial sources to generate probability density functions (PDFs) for non-detected fluxes, with the prior that the true flux must be positive. We added artificial sources with known, positive fluxes (F_{true}) in random positions across the field and then measured the PSF fluxes (F_{meas}) of these artificial sources as previously described. The distribution of F_{true} values associated with objects that have a given F_{meas} represents a PDF that can be used for assessing the uncertainty in an object's color. The resulting PDF is a Gaussian centered on F_{meas} and FWHM $\sim \sigma_{meas}$, with the negative values truncated. We therefore take the probability density function for measured flux values associated with real sources, positive and negative, to be a Gaussian with $\mu = F_x$ and $\sigma = \sigma_x$, with negative values truncated and renormalized to unity.

For simplicity, we express the color criteria as flux ratios. To find the PDF of a flux ratio, we first generate a PDF for each flux value as described above. We then take the ratio of each possible combination of values from the 1D PDFs to generate a 2D PDF for the flux ratio. We then find the total probability that the flux ratio exceeds the minimum color threshold to evaluate the selection criteria.

In addition to the color cuts described above, we also require that $F_{NB816} \geqslant 7.6F_{r2}$ (or $r2 - NB816 \geqslant 2.2$) with at least a 50% probability. This requirement follows from the $i2 - NB816$ and $r2 - i2$ colors above, and is expected due to the decreasing transmission of blue flux from high-redshift objects. This additional check helps to exclude objects with a significant probability of being low-redshift contaminants.

Finally, we adopted a narrowband limit of $NB \leqslant 25.5$. This is somewhat brighter than the limit of $NB816 \leqslant 26.0$ used by Becker et al. (2018). The brighter limit was chosen because,

after making completeness corrections (see Section 4), we found that our observations were only $\sim 10\%$ complete in the $25.5 \leqslant NB816 \leqslant 26.0$ bin. We selected an additional 143 objects in this bin, although they are excluded from the analysis because of the poor completeness.

To summarize, the final selection criteria applied to our LAEs are as follows:

1. $NB \leqslant 25.5$
2. $S/N_{NB816} \geqslant 5$
3. $\frac{F_{NB816}}{F_{i2}} \geqslant 3.0$ (50% probability) and $\frac{F_{NB816}}{F_{i2}} \geqslant 1.7$ (95% probability)
4. $F_{r2} \leqslant 2\sigma_{r2}$, or $F_{r2} \geqslant 2\sigma_{r2}$ and $F_{i2}/F_{r2} \geqslant 2.5$
5. $\frac{F_{NB816}}{F_{r2}} \geqslant 7.6$ (50% probability) and $\frac{F_{NB816}}{F_{r2}} \geqslant 4.0$ (95% probability)

Finally, objects that pass these criteria are inspected visually to remove moving or spurious sources.

To summarize, our selection criteria are based on ones used in previous works to detect LAEs at $z = 5.7$ with the Subaru (e.g., Ouchi et al. 2008, 2018; Konno et al. 2017; Shibuya et al. 2018), but with some modifications. The main differences are that we impose additional probability requirements for the color criteria and add a $\frac{F_{NB816}}{F_{r2}}$ requirement. Following Díaz et al. (2014), we also do not make use of a bluer filter to exclude low-redshift contaminants. We do, however, use a more selective $r2$ criterion than Ouchi et al. (2018) and Shibuya et al. (2018), who require that LAEs are undetected in $r2$ at 3σ (compared to 2σ in this work) unless they satisfy the $r2 - i2$ color cut.

Spectroscopic follow-up of a subset of LAEs in the J0148 field with Keck/DEIMOS suggests that our selection criteria should yield a high-quality sample of LAEs. We present details of the spectroscopy in Appendix B.

4. Results

We now turn to the results of the photometric selection. Using the procedure outlined in Section 3.2, we select 641 LAEs in the J0148 field and 428 LAEs in the J1250 field. The number of LAEs selected in the J0148 field is somewhat lower than found by Becker et al. (2018). We discuss the reasons for this difference in Appendix C, but note that the overall spatial distribution of sources is similar. Cutout images, for example, of LAE candidates selected in the J0148 field (top three rows) and J1250 field (bottom three rows) are shown in Figure 2. The cutout images are $10''$ on each side and centered on the LAE candidate. Each row shows an example candidate of a different narrowband magnitude (shown at the left) in the $r2$, $i2$, and NB816 bands (left to right). The examples were chosen to have S/N_{NB816} near the median value for objects of similar magnitude.

The surface density of the LAE candidates within $45'$ of the quasar position in both fields as a function of their NB816 magnitude is shown in Figure 3. Raw values are shown with open markers, and completeness-corrected values are shown with filled markers. We calculate the completeness correction as a function of both distance from the quasar position and NB816 magnitude by injecting a catalog of artificial LAE candidates across the field, then putting them through the LAE selection procedure. The completeness correction applied to the real LAE candidates is then given by the reciprocal of the fraction of artificial LAEs detected in each bin. The correction factor adjusts for variations in sensitivity across the field and for the loss of area covered by bright foreground sources. The completeness as a function of NB816
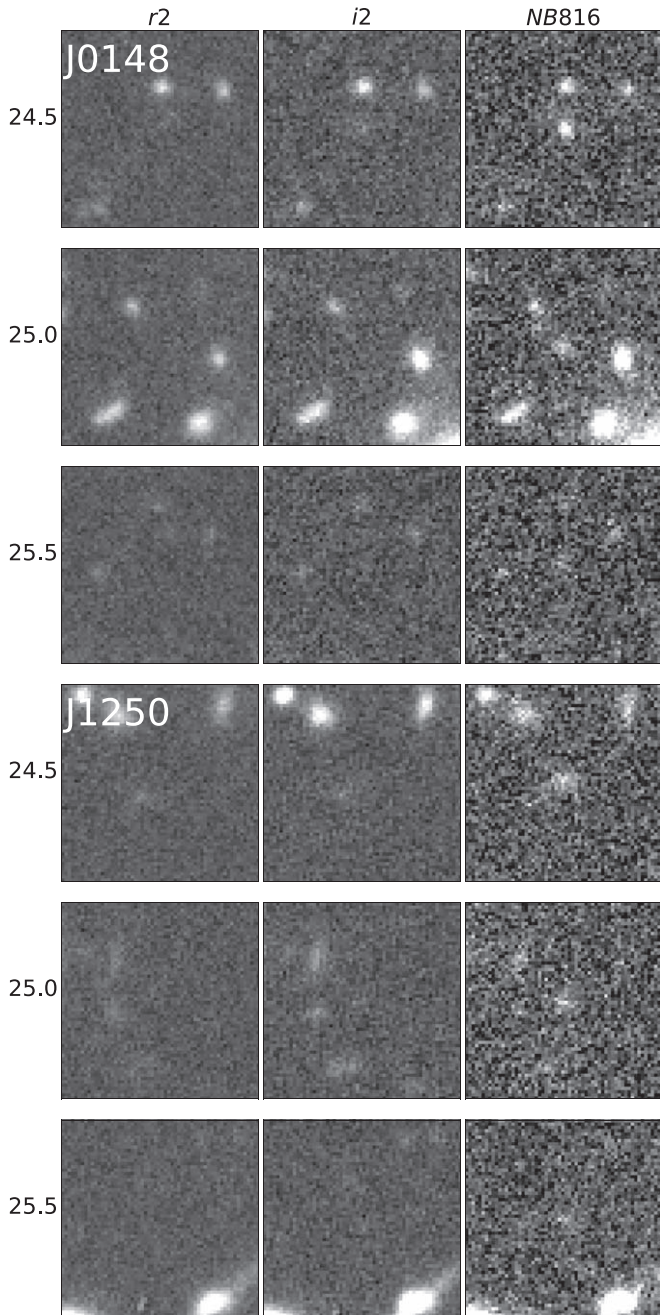
Figure 2. Example LAE candidates selected in the J0148 (top three rows) and J1250 (bottom three rows) fields with the criteria described in Section 3.2. The cutout images are 10″ on each side and centered on the LAE position. Each row shows images of a sample candidate of a different narrowband magnitude (shown at the left) in the $r2$, $i2$, and NB816 bands (left to right). The sample candidates were chosen to have S/N$_{NB816}$ values near the median for objects at similar NB816 magnitudes.

magnitude and distance from the quasar for both fields is given in Appendix D.

The spatial distribution of selected LAEs in each field is shown in Figure 4. LAE candidates are shown with colors corresponding to their NB816 magnitudes. The quasar is centered in each field and denoted with a star. Dotted, concentric circles are plotted in increments of $10\ h^{-1}$ Mpc. The solid outer circle shows the edge of the field of view, 45′ from the quasar.

LAE candidates are shown plotted over a surface density map. We create the surface density map for the LAE candidates in each field by superimposing a regular grid of 0′.24 (0.4 h^{-1} Mpc)

pixels onto the field. In each grid cell, we find the surface density by kernel density estimation using a Gaussian kernel of bandwidth 0′.15. We then normalize the grid by the average surface density of the field.

We calculate the surface density of the LAE candidates as a function of the radius. The raw surface density is measured in $10\ h^{-1}$ Mpc concentric annuli centered on the quasar position and then corrected for completeness. The corrected surface density is shown as a function of projected distance from the quasar for each field in Figure 5. The horizontal line represents the mean background surface density of LAE candidates, averaged over $15' \leqslant \Delta\theta \leqslant 40'$. The surface density measurements for the J0148 and J1250 fields are summarized in Tables 2 and 3, respectively.

The key result from Becker et al. (2018) is unchanged; Figure 4 shows a marked underdensity within 20 h^{-1} Mpc of the quasar in the J0148 field. The LAE catalog presented here and that presented in Becker et al. (2018) are largely consistent within the expected variations in LAE selection at the faintest magnitudes, where the sample is ∼50% complete, and display the same large-scale structures. We estimate that 15% of the objects appearing in each catalog are affected by the flux issues discussed in Section 3.1. A more detailed comparison is given in Appendix C.

We also find a deficit of LAEs in the inner 20 h^{-1} Mpc of the J1250 field. This result is consistent with the J0148 field, and confirms the association between highly opaque sightlines and underdense regions in a second field.

We note that the two fields vary in the observed surface density of LAEs; we select 641 LAEs in the J0148 field and 428 in the J1250 field in the same survey volume. While our main result is based on a differential measurement of the LAE surface density *within* each field, one might also wonder about the variance in LAE density *between* the two fields. We can gauge whether this variance is reasonable by using a simple linear bias treatment, which is accurate for the large volume probed by our survey (see, e.g., Trapp & Furlanetto 2020). Using the Trac et al. (2015) halo mass function and its linear bias expansion with the standard scaling method (Tramonte et al. 2017; Trapp & Furlanetto 2020), we expect $\sim 535 \pm 100$ halos of mass $\sim 1.7 \times 10^{11}\ M_\odot$ dark matter halos in each of our fields, where the error is the 1σ sample variance. In this scenario, the two fields are within $\sim 1\sigma$ of the expected value. If, however, only one-quarter of halos contain LAEs, the number density would correspond to $7 \times 10^{10}\ M_\odot$ halos, which have a fractional standard deviation due to the sample variance of ∼0.16, still consistent with the observed fields. Both of these scenarios are reasonable in light of the independent measurements of the LAE properties at $z \sim 6$. For example, Khostovan et al. (2019) estimate halo masses $\sim 10^{11}\ M_\odot$ for LAEs via clustering, while Stark et al. (2010) find that ∼25%–50% of galaxies have strong Lyα emission lines.

Gangolli et al. (2021) similarly find that large-scale structure is sufficient to explain the significant field-to-field variations of $z = 5.7$ LAEs in the SILVERRUSH survey (Ouchi et al. 2018). In contrast, they argue that patchy reionization is unlikely to drive these variations because, at the end of reionization, the neutral gas is largely confined to voids, where it should obscure fewer galaxies. We note that our fields are somewhat unusual in that they were selected to have high IGM Lyα opacities at the field center. Even so, the overall variation in number mean density between fields appears to be consistent with cosmic variance in the number density of LAE hosts at this redshift.
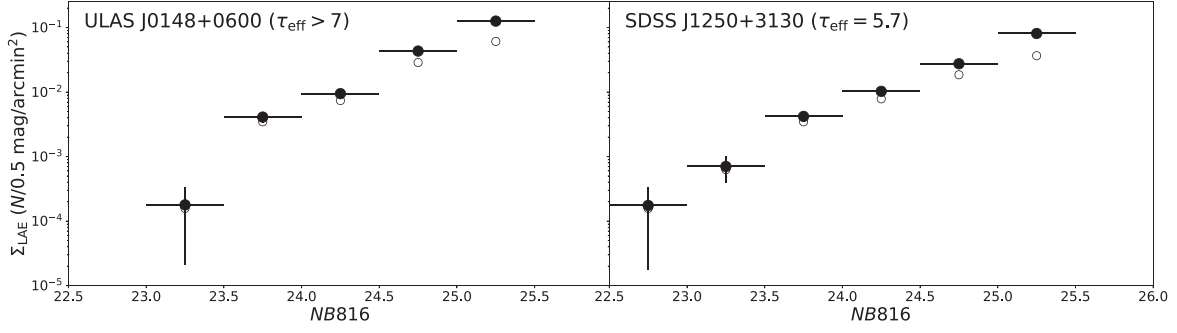
Figure 3. Surface density of LAE candidates in the J0148 (left) and J1250 (right) fields. The LAE candidates are binned in 0.5 mag increments. Raw surface densities are shown with open markers. Filled markers show the surface densities with a correction made for completeness (see Section 4 and Appendix D). The error bars on the corrected measurements are 68% Poisson intervals.
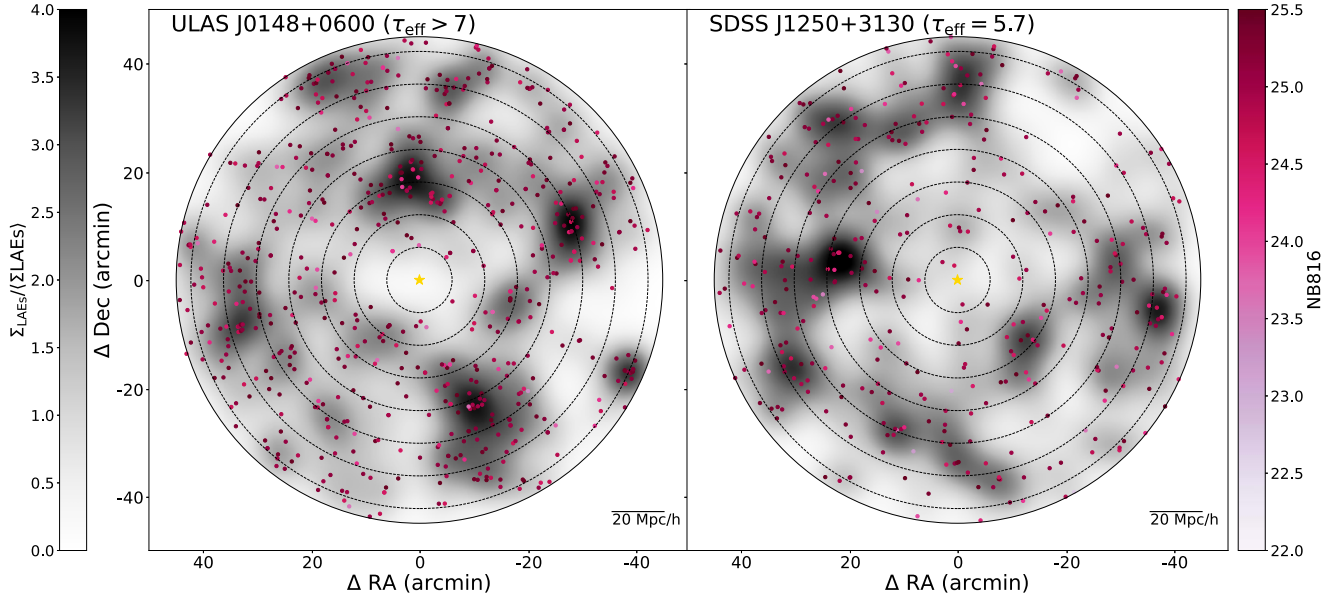
Figure 4. Distribution of LAE candidates in the J0148 (left) and J1250 (right) fields. Each field is shown centered on the quasar (gold star). LAE candidates are shown with a color that indicates their narrowband magnitude. Shading indicates the surface density of LAE candidates at each position, which is calculated by kernel density estimation using a Gaussian kernel and normalized by the mean surface density measured across the entire field. Concentric, dotted circles are shown in increments of $10\ h^{-1}$ Mpc projected distance from the quasar. The solid circle marks the edge of the field of view, $45'$ from the quasar.
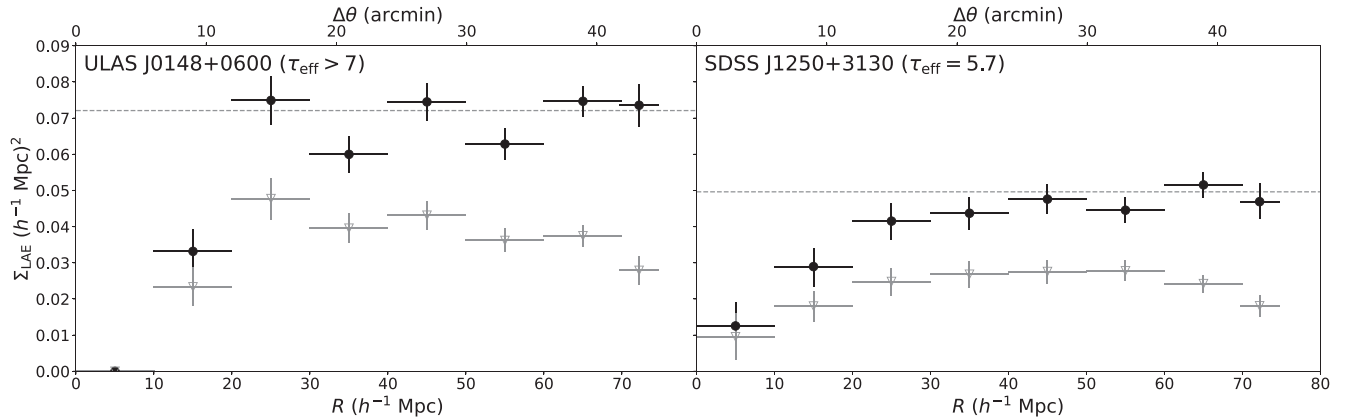
Figure 5. Surface density of LAEs in the J0148 (left) and J1250 (right) fields. The filled black circles show corrected surface density, and the unfilled gray triangles show the uncorrected measurements. The surface density is measured as a function of projected distance from the quasar in annual bins of $10\ h^{-1}$ Mpc, except for the outermost bin which is $4.5\ h^{-1}$ Mpc. The dotted line represents the mean surface density of LAE candidates that lie within $15' \leqslant \Delta\theta \leqslant 40'$ of the quasar. Horizontal error bars show the width of the annuli, and vertical error bars are 68% Poisson intervals.

Table 2
LAE Number Density in the J0148 Field

R (Mpc)	N_{LAEs}	N_{corr}[a]	Σ LAE (Mpc $h^{-1})^2$
5 (0–10)	0	0	0.00
15 (15–25)	22	31	0.033 (0.028–0.039)
25 (20–30)	75	118	0.075 (0.068–0.081)
35 (30–40)	87	132	0.060 (0.055–0.065)
45 (40–50)	122	211	0.075 (0.069–0.080)
55 (50–60)	125	217	0.063 (0.058–0.067)
65 (60–70)	153	305	0.075 (0.071–0.079)
72 (70–74.5)	57	150	0.074 (0.68–0.079)

Note.
[a] Completeness corrected.

Table 3
LAE Number Density in the J1250 Field

R (Mpc)	N_{LAEs}	N_{corr}[a]	Σ LAE (Mpc $h^{-1})^2$
5 (0–10)	3	4	0.013 (0.006–0.019)
15 (15–25)	17	27	0.030 (0.023–0.034)
25 (20–30)	39	65	0.042 (0.036–0.046)
35 (30–40)	59	96	0.044 (0.039–0.048)
45 (40–50)	78	135	0.048 (0.043–0.052)
55 (50–60)	96	154	0.045 (0.041–0.048)
65 (60–70)	99	210	0.052 (0.048–0.055)
72 (70–74.5)	37	196	0.047 (0.042–0.052)

Note.
[a] Completeness corrected.

5. Analysis

5.1. Comparison to Models for Opaque Sightlines

We now compare our observations to models that attempt to explain the large-scale fluctuations in IGM Lyα opacity at $z \lesssim 6$. We consider six variations on three main types of models: fluctuating UVB, fluctuating temperature, and ultra-late reionization. We refer the reader to the introduction for a more detailed description of these models.

The first type of model is defined by large-scale fluctuations in the UVB. We consider two galaxy-driven models, one from Davies & Furlanetto (2016) and one from Nasir & D'Aloisio (2020). In these models, UVB fluctuations are driven by the clustering of ionizing sources and a short, spatially variable mean free path. The Nasir & D'Aloisio (2020) model is based on an *early* (completed by $z \simeq 6$) reionization simulation and also includes temperature fluctuations. In these models, high-opacity lines of sight are typically associated with underdense regions, where the UVB is suppressed. We also consider a quasar-driven UVB model based on Chardin et al. (2015, 2017). In this model, high-opacity lines of sight may be associated with a wide range of densities provided that they are in regions far from quasars, where the UVB is low. We note that this model is disfavored by the fact that quasars may only provide a small fraction of the UVB at these redshifts (e.g., McGreer et al. 2018; Parsa et al. 2018; Kulkarni et al. 2019b), but consider it here for completeness.

The second type of model is from D'Aloisio et al. (2015), and is defined by large-scale temperature fluctuations. In this model, highly opaque lines of sight are associated with overdensities that reionized early and have had sufficient time to cool.

The third type of model is defined by reionization being incomplete at $z = 6$. We consider two ultra-late reionization models

from Nasir & D'Aloisio (2020). These models include both regions of neutral hydrogen and a fluctuating ionizing background driven by clustered ionizing sources and a finite mean free path. At $z = 5.8$, the "long mean free path" model has a hydrogen neutral fraction of $\langle \chi_{\mathrm{H\,I}} \rangle = 0.14$ and a mean free path of $\langle \lambda_{\mathrm{mfp}} \rangle = 27\ h^{-1}$ Mpc, while the "short mean free path" model has $\langle \chi_{\mathrm{H\,I}} \rangle = 0.10$ and $\langle \lambda_{\mathrm{mfp}}^{912} \rangle = 9\ h^{-1}$ Mpc. Predictions for the late reionization models in Nasir & D'Aloisio (2020) are qualitatively consistent with those from Keating et al. (2020b) for opaque lines of sight.

Predictions for the Nasir & D'Aloisio (2020) models are taken directly from that work. All others are as implemented in Becker et al. (2018). The LAE modeling is done using a similar approach in all cases. We refer the reader to these papers for details, but briefly summarize the method here. Galaxies are assigned to dark matter halos via abundance matching to the measured UV luminosity function of Bouwens et al. (2015). The spectra are modeled with a power-law continuum and a Lyα emission line, with rest-frame equivalent widths drawn from the empirically calibrated models of Dijkstra & Wyithe (2012). The modeled LAE populations are then used to construct the expected surface density profiles for highly opaque lines of sight. Becker et al. (2018) use sightlines with $\tau_{\mathrm{eff}} \geqslant 7$ measured on 50 h^{-1} Mpc scales. This scale is somewhat shorter than the lengths of the J0148 and J1250 troughs (110 h^{-1} Mpc and 81 h^{-1} Mpc respectively); however, Davies et al. (2018a) compared predictions for the surface density of LAEs as a function of τ_{eff} on both 50 h^{-1} and 110 h^{-1} Mpc scales and found that the predictions were not highly sensitive to this choice. Nasir & D'Aloisio (2020) use the 100 longest troughs in each simulation to make their predictions, typically $80-100\ h^{-1}$ Mpc in length, which is comparable to the lengths of the J0148 and J1250 troughs.

We compare these model predictions to the measured LAE surface density in the J0148 and J1250 fields in Figure 6. The top panel shows, from left to right, the galaxy UVB model based on Davies & Furlanetto (2016), the QSO UVB model based on Chardin et al. (2017), and the fluctuating temperature model based on D'Aloisio et al. (2015). The lower panel shows the three models from Nasir & D'Aloisio (2020): the first (left) is a galaxy UVB model, the second (center) is the ultra-late reionization scenario with a long mean free path, and the third (right) is the ultra-late reionization scenario with a short mean free path.

The predictions from each model are averaged over 10 h^{-1} Mpc bins. The solid lines show the median prediction. In the top panels, the dark- and light-shaded regions indicate the 68% and 95% ranges, respectively, subtended by the mock samples drawn from the simulation. In the lower panel, the shaded regions indicate the tenth and ninetieth percentiles. All surface densities are normalized by the mean surface density in the field measured over $15 \leqslant \theta \leqslant 40$. We note that these model predictions are made for sightlines with $\tau_{\mathrm{eff}} \geqslant 7$, while the J1250 sightline has $\tau_{\mathrm{eff}} \simeq 6$. Davies et al. (2018a), however, find that the predictions for these opacities are very similar.

In both the J0148 and J1250 fields, we observe a decrease in LAE surface density within 20 h^{-1} Mpc of the quasar. As shown in Figure 6, this deficit of LAEs surrounding highly opaque lines of sight is consistent with the galaxy UVB and late reionization models, but strongly disfavors the temperature model. We thus demonstrate that the association between high Lyα opacity and low galaxy density first reported by Becker et al. (2018) extends to at least two fields. While Becker et al. (2018) considered only the fluctuating UVB and temperature models, moreover, here we show that the observed opacity-density
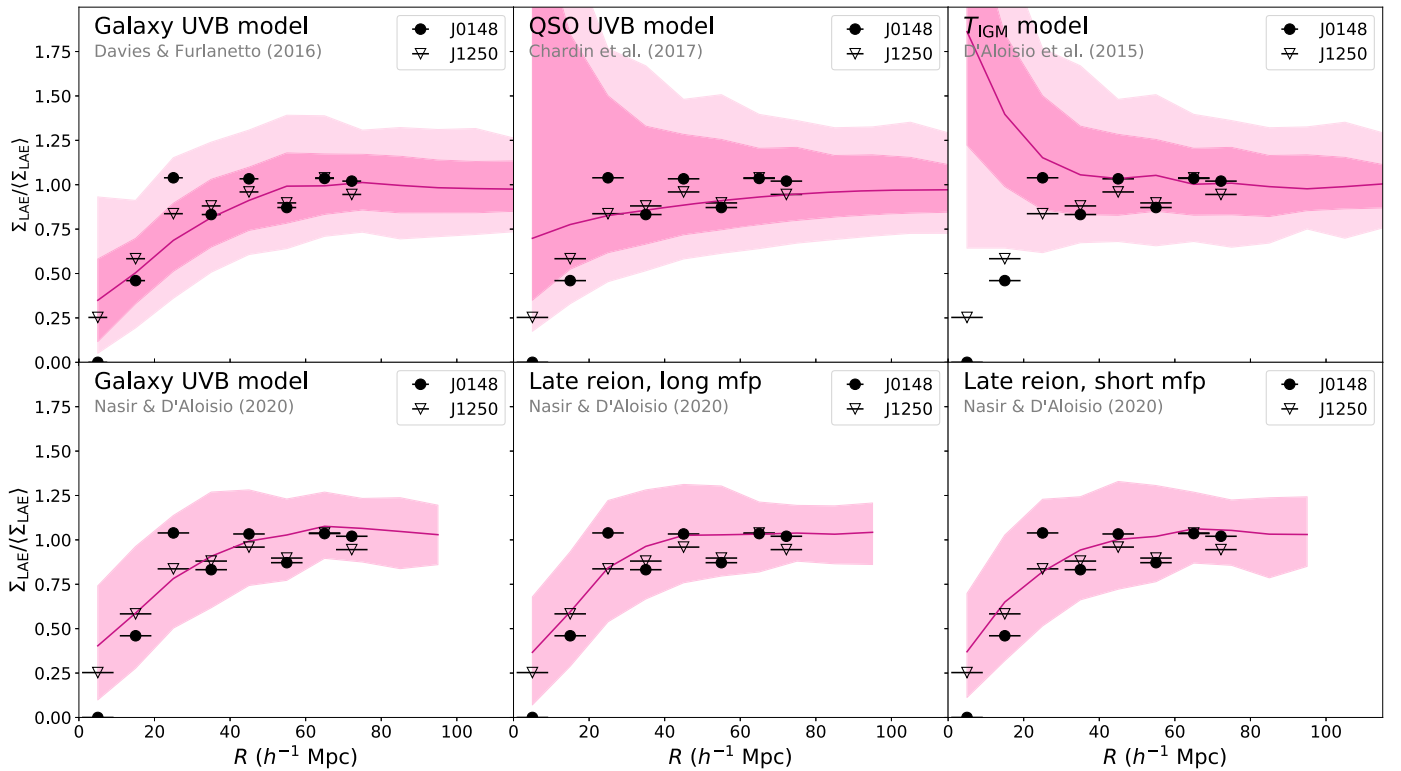
Figure 6. Comparison of the observed radial distribution of LAE candidates in the J0148 (filled circles) and J1250 (open triangles) fields to model predictions. The top row shows predictions from the galaxy UVB model based on Davies & Furlanetto (2016; top left), the QSO UVB model based on Chardin et al. (2015, 2017; top center), and the fluctuating temperature model from D'Aloisio et al. (2015; top right). The bottom row shows predictions from Nasir & D'Aloisio (2020), including their galaxy UVB (early reionization) model (bottom left), late reionization model with a long mean free path (bottom center), and late reionization model with a short mean free path (bottom right). All model predictions are for highly opaque lines of sight ($\tau_{\rm eff} \geqslant 7$). The horizontal error bars on the measured data points indicate the width of the bins, which is 10 h^{-1} Mpc for all except the outermost bin, which is 4.5 h^{-1} Mpc. The solid lines show median model predictions, which are averaged over 10 h^{-1} Mpc bins throughout the simulation. In the top panels, the dark- and light-shaded regions show 68% and 95% ranges subtended by the mock samples drawn from the simulation. The shaded regions in the lower panels show the 90% range. All surface densities are given as a fraction of the mean surface density measured over $15' \leqslant \theta \leqslant 40'$.

relation is consistent with models where reionization extends to $z < 6$.

6. Summary

We present a selection of LAEs using the Subaru HSC narrowband imaging in the fields surrounding two highly opaque quasar sightlines, toward ULAS J0148+0600 ($\tau_{\rm eff} \geqslant 7$) and SDSS J1250+3130 ($\tau_{\rm eff} = 5.7 \pm 0.4$). The observations establish the LAE density expected in the vicinity of two giant Lyα troughs, which we use to test IGM models that predict a relationship between opacity and density. The results for the J0148 field are an update to those previously reported by Becker et al. (2018), here using improved photometric measurements and more stringent LAE selection criteria. Observations of the J1250 field are presented here for the first time.

In both fields, we find a deficit of LAEs within 20 h^{-1} Mpc of the quasar sightline. This confirms the results of Becker et al. (2018) in the J0148 field, and demonstrates in a second field that long, highly opaque Lyα troughs are associated with underdense regions as traced by LAEs.

These observations provide a direct test of three major types of models that attempt to reproduce the large-scale scatter in Lyα opacity at $z \simeq 5.5$–6: fluctuating ultraviolet background models, where the UVB is produced either by galaxies (Davies & Furlanetto 2016; D'Aloisio et al. 2018; Nasir & D'Aloisio 2020) or quasars (Chardin et al. 2015, 2017); the fluctuating temperature model (D'Aloisio et al. 2015); and ultra-late reionization models

(Kulkarni et al. 2019a; Keating et al. 2020a, 2020b; Nasir & D'Aloisio 2020). Our results disfavor the temperature model but are consistent with predictions made by the galaxy-driven UVB models, in which highly opaque troughs correspond to low-density regions with a suppressed ionizing background. The results are also consistent with ultra-late reionization models, in which long troughs arise from the last remaining islands of neutral hydrogen, which are also predicted to occur in low-density regions. There is some overlap between these two types of models, as the ultra-late reionization models also include strong UVB fluctuations. The ultra-late reionization model is distinguished by the presence of neutral islands at $z < 6$.

Our results are consistent with a number of recent observations that point toward a late and rapid reionization scenario that has its midpoint at $z \sim 7$–8 and ends at $z \leqslant 6$. A growing body of work is reconsidering the long-standing conclusion that reionization was complete by $z = 6$ (e.g., Kulkarni et al. 2019a; Nasir & D'Aloisio 2020; Keating et al. 2020a, 2020b; Choudhury et al. 2021; Qin et al. 2021), and therefore discriminating between late reionization and fluctuating UVB models is of great interest.

This work has focused on fields surrounding highly opaque lines of sight, but further insight may come from fields at the opposite extreme of Lyα opacity. The UVB models predict that highly transmissive sightlines should be associated with galaxy overdensities producing a strong ionizing background (Davies et al. 2018a). In contrast, the late reionization models predict that, in some cases, transmissive sightlines should be associated

with low-density regions that have been recently reionized (Keating et al. 2020b), and may generally arise from a range of overdensities (Nasir & D'Aloisio 2020). Establishing the density field surrounding highly transmissive sightlines may, therefore, prove to be a useful test of these competing models.

Appendix A
Lyα Opacity of Quasar Sightlines

As done by Becker et al. (2018), we use our imaging data to estimate $\tau_{\rm eff}$ along both quasar lines of sight using the PSF photometry described in Section 3.1. The purpose of these measurements is to check whether our data are consistent with existing spectroscopic limits for these sightlines and whether it is possible to improve on the existing limits given the depth of our data. For each quasar, we first measure the NB816 and $i2$ fluxes. We then convolve each object's spectrum with the $i2$ transmission curve, and scale the spectrum so that its transmission-weighted mean flux over the $i2$ band matches what was measured in the imaging. We use the scaled spectrum to estimate the unabsorbed continuum flux at the narrowband wavelength, and then using the photometric narrowband flux we calculate the effective opacity as $\tau_{\rm eff} = -\ln(F_\lambda^{\rm NB816}/F_\lambda^{\rm cont})$. These measurements represent an effective opacity over the NB816 wavelength region, which is overlapped by but considerably shorter than the spectroscopically-measured regions of both troughs.

In the J0148 sightline, we measure $F_\lambda^{\rm NB816} = (2.0 \pm 1.8) \times 10^{-20}$ erg s^{-1} cm^{-2} Å^{-1} and $F_\lambda^{i2} = (3.2 \pm 0.5) \times 10^{-18}$ erg s^{-1} cm^{-2} Å^{-1}, and estimate that the unabsorbed continuum is $F_\lambda^{\rm cont} = 1.5 \times 10^{17}$ erg s^{-1} cm^{-2} Å^{-1}. Therefore, we measure $\tau_{\rm eff} = 6.63^{+2.5}_{-0.65}(1\sigma)$, or a 2σ lower limit of $\tau_{\rm eff} \geqslant 5.59$, which is consistent with the 2σ lower limit, measured by Becker et al. (2015), of $\tau_{\rm eff} \geqslant 7.2$ measured over a 50 h^{-1} Mpc section centered at $z = 5.726$.

The J1250 quasar is not detected in our NB816 data. As a rough estimate, we adopt the 2σ upper limit, $F_\lambda^{\rm NB816} \leqslant 4.0 \times 10^{-20}$ erg s^{-1} cm^{-2} Å^{-1}. We also measure $F_\lambda^{i2} = (7.3 \pm 0.2) \times 10^{-19}$ erg s^{-1} cm^{-2} Å^{-1}, and estimate that the unabsorbed continuum is $F_\lambda^{\rm cont} = 1.0 \times 10^{17}$ erg s^{-1} cm^{-2} Å^{-1}. Therefore, we measure $\tau_{\rm eff} \geqslant 5.52^{+0.69}_{-0.41}(1\sigma)$, or a 2σ lower limit of $\tau_{\rm eff} \geqslant 4.83$. This measurement is consistent with that of Zhu et al. (2021), who find that $\tau_{\rm eff} = 5.7 \pm 0.4$ measured over 81 h^{-1} Mpc centered at $z = 5.760$.

Appendix B
Spectroscopic Follow-up of J0148 LAEs with Keck/ DEIMOS

B.1. Observations

In addition to the imaging data discussed in Section 2, we obtained spectra of 46 LAE candidates in the J0148 field taken with the DEIMOS spectrograph (Faber et al. 2003) on the Keck II telescope in 2018 November. Targets were selected from the catalog of LAE candidates published in Becker et al. (2018), as spectroscopic follow-up was carried out prior to the creation of the catalog presented in this work. We prioritized objects in the underdense region at the center of the field of view, a second low-density region at the west edge of the field, and a high-density region. In total we used five masks, which we designed using DSIMULATOR (Figure 7). The observations, which are summarized in Table 4, were made in multi-slit mode using the OG550 filter and the 600-line grating. Each individual target
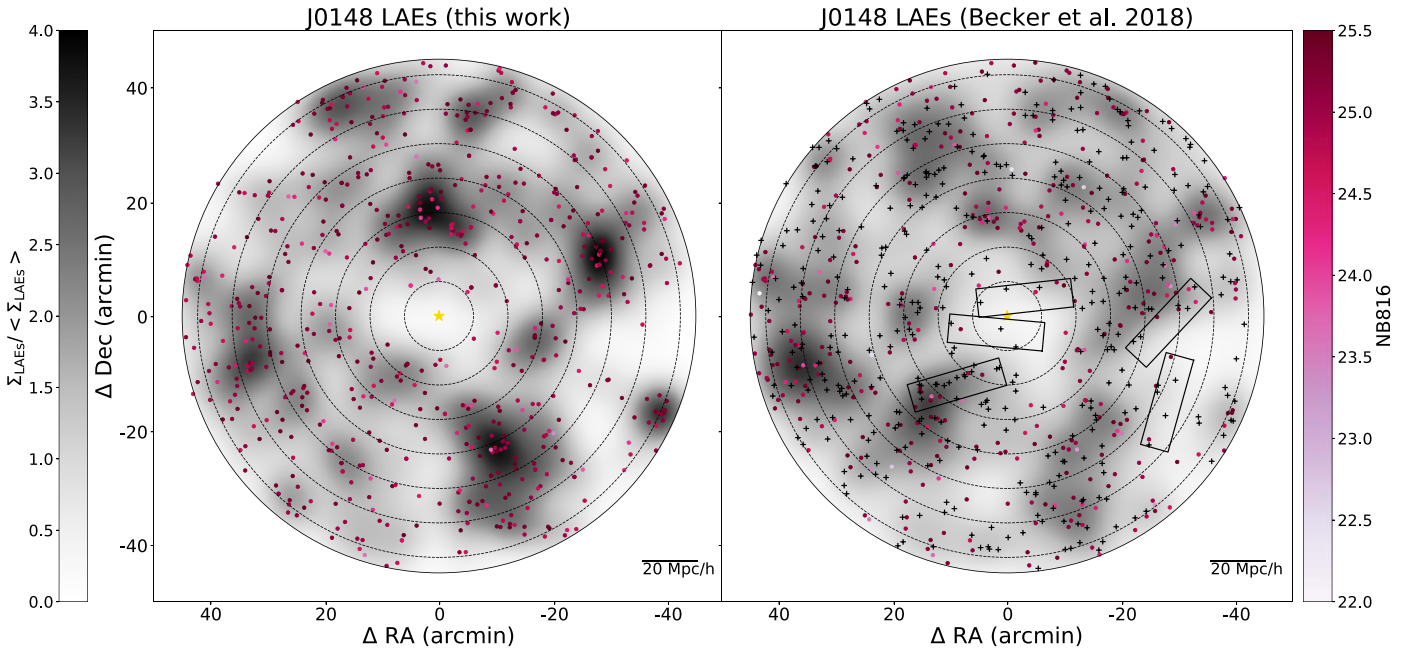
Figure 7. Distribution of LAE candidates in the J0148 field as selected in this work (left) and by Becker et al. (2018; right). Each field is shown centered on the quasar (gold star). LAE candidates with NB816 < 25.5 are shown with a color that indicates their narrowband magnitude in their respective catalog. In the right panel, LAEs selected in Becker et al. (2018) with NB816 > 25.5 (fainter than our selection limit) are shown with black crosses. The surface density at each position is calculated by kernel density estimation using a Gaussian kernel, and is normalized by the mean surface density measured across the entire field. Concentric, dotted circles are shown in increments of 10 Mpc h^{-1} projected distance from the quasar. The black rectangles in the right panel indicate the pointings of DEIMOS slitmasks used for spectroscopic follow-up. The solid circle marks the edge of the field of view, 45′ from the quasar.

Table 4
Summary of Keck/DEIMOS Observations

Date	Mask[a]	Description	t_{exp} (h)	Seeing[b]
11/28/18	1	Central	2	0″.74
11/28/18	2	Central	2	0″.73
11/29/18	3	High Density	2	0″.83
11/29/18	4	High Density	2	0″.65
11/28–11/29	5	Low Density	1.2	0″.78

Notes.
[a] The first priority for mask placement was to maximize the number of LAE candidates observed within 20 h^{-1} Mpc of the quasar. Masks were also placed to cover other high- and low-density regions of the field.
[b] Median seeing measured from Gaussian fits to the profiles of stars on each mask.

was placed in a 1″ slit, and all slits were tilted five degrees relative to the position angle of the mask in order to better sample the sky lines for sky subtraction.

We reduced the raw spectra with a custom IDL pipeline that includes optimal sky subtraction (Kelson 2003). Individual exposures were then combined onto a 2D grid rectified with nearest neighbor resampling, in which each frame's individual pixels are assigned to the pixel in the combined frame that it most closely matches in position and wavelength. Rectifying the spectra in this way ensures that pixels in the combined frame remain uncorrelated. Finally, we corrected the spectra for atmospheric absorption, and flux calibrated using standard stars.

B.2. Results

Emission lines were identified by visual inspection of the 2D spectra. To be spectroscopically confirmed, an LAE candidate
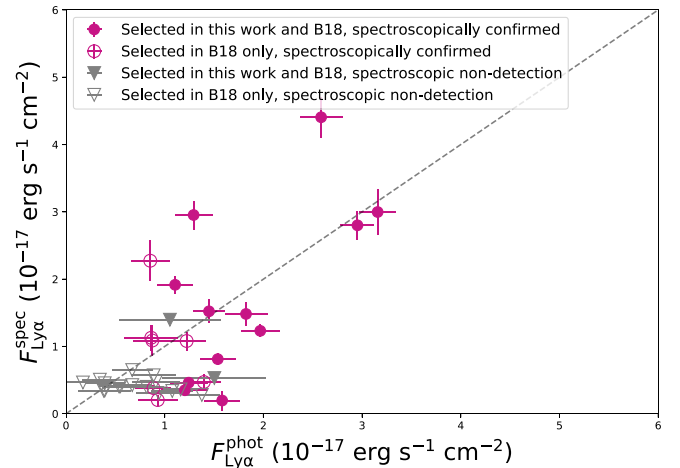

Figure 8. Photometric and spectroscopic fluxes for all the credible LAE candidates. The following objects are considered credible: all the spectroscopically confirmed objects, the spectroscopic non-detections that were selected photometrically in this work, and the non-detections that were selected only by Becker et al. (2018) that also passed a secondary visual inspection to remove clearly spurious sources. Spectroscopically confirmed LAEs are shown with circles, and the spectroscopic non-detections are shown with triangles. LAEs that meet the photometric criteria outlined in 3.2 are shown with filled markers; LAEs that fail one or more photometric criteria are shown with empty markers. For the spectroscopic non-detections, the reported flux is a 1σ upper limit.

was required to have a single emission line in the Lyα region, and no emission lines were elsewhere in the trace. For each spectroscopically confirmed LAE, we determine the spectroscopic redshift from the flux-weighted mean wavelength of the emission line, which is calculated over a 20 Å window centered on the visually-estimated line center. This window was chosen to be wide enough to cover any of the emission lines in our sample, but not so wide as to include unwanted skyline noise. We also
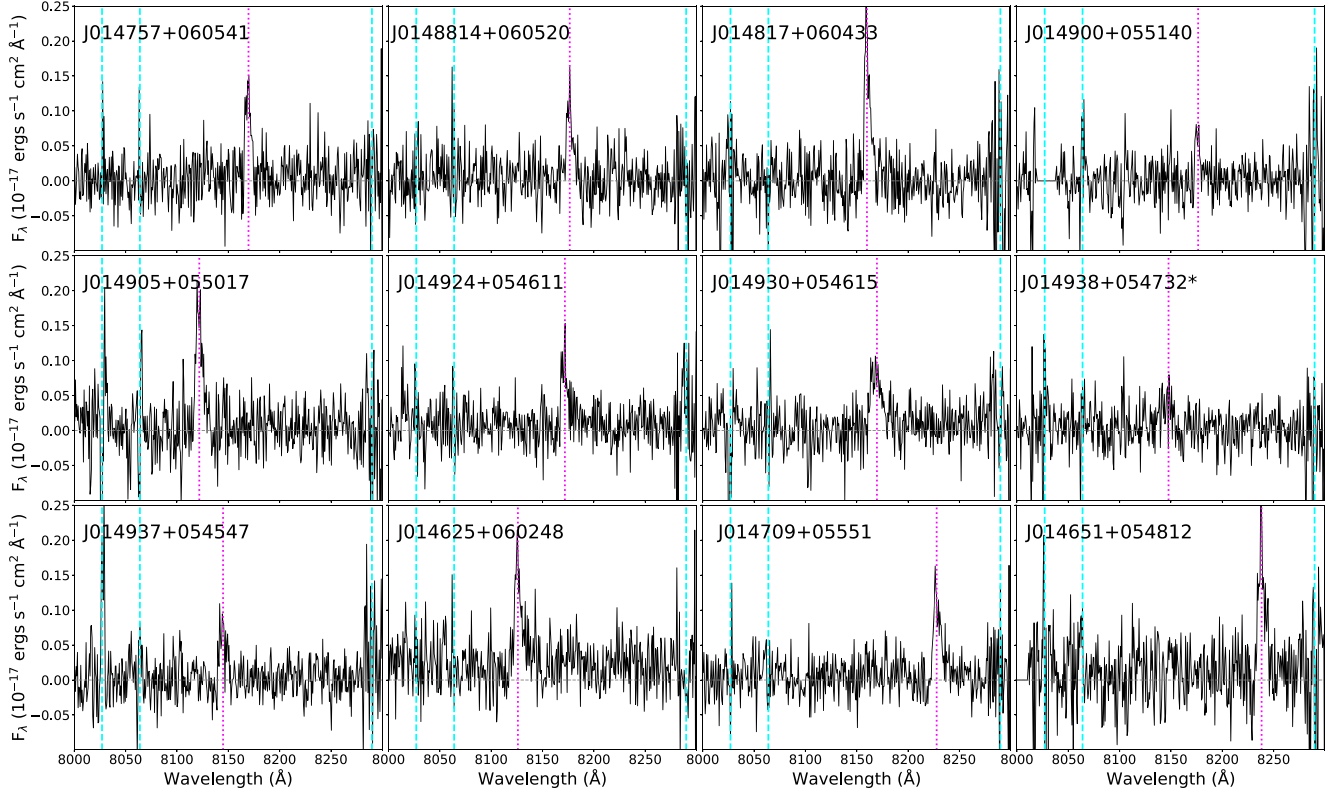
Figure 9. Spectra for each of the spectroscopically confirmed LAEs that meet the photometric criteria outlined in 3.2. The dashed cyan lines indicate skyline residuals, while the dotted pink line indicates the flux-weighted mean wavelength of the emission line, which is used to calculate the spectroscopic redshift. J0149938+054732 (marked with an asterisk) is a marginal detection with 1.4σ confidence.
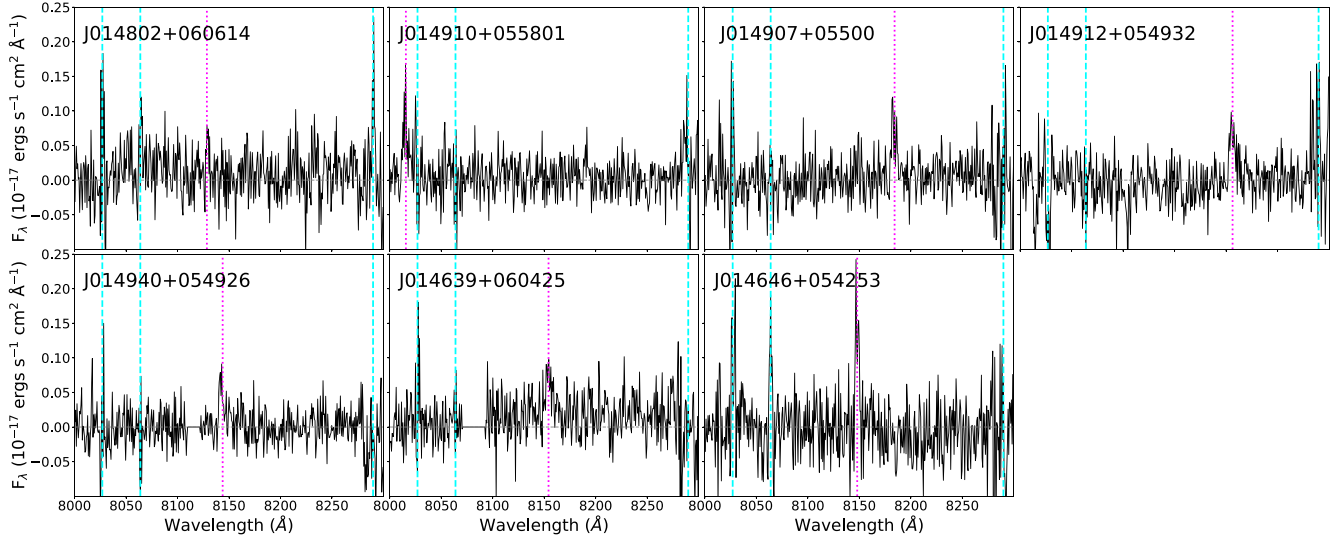
Figure 10. Spectra for each of the spectroscopically confirmed LAEs that were selected in Becker et al. (2018) but were not selected by the photometric criteria outlined in Section 3.2. The dashed cyan lines indicate skyline residuals, and the dotted pink line indicates the flux-weighted mean wavelength of the emission line, which is used to calculate the spectroscopic redshift.

measure the Lyα flux by integrating the spectrum over a wavelength region that includes the entire emission line; this region is customized for each object, but is typically ∼15 Å. Table 5 summarizes the properties of all spectroscopically confirmed LAEs. We compare the photometric and spectroscopic Lyα fluxes for all the credible LAEs in Figure 8, which includes the spectroscopically confirmed objects, the spectroscopic non-

detections that were selected photometrically in this work, and the non-detections that were selected only by Becker et al. (2018) that also passed a secondary visual inspection to remove clearly spurious sources. Figure 8 demonstrates a reasonable agreement between the photometric and spectroscopic measurements, including for the spectroscopic non-detections, which tend to be the faintest objects in the sample.

Table 5
Summary of All Spectroscopically Confirmed LAEs in the J0148 Field

ID	R.A. (J200)	Decl. (J1200)	$z_{\rm spec}$	$m_{\rm NB816}$[a] (mag)	$F_{\rm phot} \cdot 10^{17}$	$F_{\rm spec} \cdot 10^{17}$	Selected?[c]
J014757+060541	$01^{\rm h}47^{\rm m}57\overset{\rm s}{.}824$	$+06^{\rm d}05^{\rm m}41\overset{\rm s}{.}87$	5.72	25.12	1.54 ± 0.18	0.81 ± 0.08	Y
J014802+060614	$01^{\rm d}48^{\rm m}02\overset{\rm s}{.}906$	$+06^{\rm d}06^{\rm m}14\overset{\rm s}{.}46$	5.69	25.67	0.93 ± 0.2	0.2 ± 0.08	N
J0148814+060520	$01^{\rm h}48^{\rm m}14\overset{\rm s}{.}932$	$+06^{\rm d}05^{\rm m}20\overset{\rm s}{.}174$	5.73	25.19	1.45 ± 0.16	1.52 ± 0.17	Y
J014817+060433	$01^{\rm h}48^{\rm m}17\overset{\rm s}{.}678$	$+06^{\rm d}04^{\rm m}33\overset{\rm s}{.}38$	5.71	24.42	2.95 ± 0.17	2.8 ± 0.21	Y
J014910+055801	$01^{\rm h}49^{\rm m}10\overset{\rm s}{.}161$	$+05^{\rm d}58^{\rm m}01\overset{\rm s}{.}87$	5.59	25.23	1.4 ± 0.18	0.47 ± 0.11	N
J014900+055140	$01^{\rm h}49^{\rm m}00\overset{\rm s}{.}853$	$+05^{\rm d}51^{\rm m}40\overset{\rm s}{.}93$	5.73	25.39	1.2 ± 0.23	0.35 ± 0.07	Y
J014905+055017	$01^{\rm h}49^{\rm m}05\overset{\rm s}{.}023$	$+05^{\rm d}50^{\rm m}17\overset{\rm s}{.}85$	5.68	24.56	2.58 ± 0.21	4.41 ± 0.3	Y
J014907+05500	$01^{\rm h}49^{\rm m}07\overset{\rm s}{.}708$	$+05^{\rm d}50^{\rm m}01\overset{\rm s}{.}74$	5.73	25.75	0.86 ± 0.27	1.13 ± 0.19	N
J014912+054932	$01^{\rm h}49^{\rm m}12\overset{\rm s}{.}801$	$+05^{\rm d}49^{\rm m}32\overset{\rm s}{.}61$	5.75	25.37	1.22 ± 0.19	1.08 ± 0.14	N
J014924+054611	$01^{\rm h}49^{\rm m}24\overset{\rm s}{.}820$	$+05^{\rm d}46^{\rm m}11\overset{\rm s}{.}47$	5.72	24.94	1.82 ± 0.21	1.48 ± 0.17	Y
J014930+054615	$01^{\rm h}49^{\rm m}30\overset{\rm s}{.}632$	$+05^{\rm d}46^{\rm m}15\overset{\rm s}{.}74$	5.72	24.34	3.16 ± 0.18	3.0 ± 0.34	Y
J014940+054926	$01^{\rm h}49^{\rm m}40\overset{\rm s}{.}087$	$+05^{\rm d}49^{\rm m}26\overset{\rm s}{.}15$	5.70	25.72	0.89 ± 0.18	0.38 ± 0.04	N
J014938+054732[b]	$01^{\rm h}49^{\rm m}38\overset{\rm s}{.}827$	$+05^{\rm d}47^{\rm m}32\overset{\rm s}{.}37$	5.70	25.09	1.58 ± 0.18	0.2 ± 0.14	Y
J014937+054547	$01^{\rm h}49^{\rm m}37\overset{\rm s}{.}493$	$+05^{\rm d}45^{\rm m}47\overset{\rm s}{.}48$	5.70	25.36	1.24 ± 0.19	0.46 ± 0.05	Y
J014625+060248	$01^{\rm h}46^{\rm m}25\overset{\rm s}{.}501$	$+06^{\rm d}02^{\rm m}48\overset{\rm s}{.}51$	5.69	24.86	1.97 ± 0.2	1.23 ± 0.09	Y
J014639+060425	$01^{\rm h}46^{\rm m}39\overset{\rm s}{.}395$	$+06^{\rm d}04^{\rm m}25\overset{\rm s}{.}49$	5.71	25.76	0.85 ± 0.19	2.27 ± 0.3	N
J014709+05551	$01^{\rm h}47^{\rm m}09\overset{\rm s}{.}103$	$+05^{\rm d}55^{\rm m}51\overset{\rm s}{.}99$	5.77	25.48	1.11 ± 0.18	1.92 ± 0.13	Y
J014651+054812	$01^{\rm h}46^{\rm m}51\overset{\rm s}{.}818$	$+05^{\rm d}48^{\rm m}12\overset{\rm s}{.}57$	5.78	25.31	1.29 ± 0.19	2.95 ± 0.21	Y
J014646+054253	$01^{\rm h}46^{\rm m}46\overset{\rm s}{.}656$	$+05^{\rm d}42^{\rm m}53\overset{\rm s}{.}31$	5.70	25.74	0.87 ± 0.19	1.09 ± 0.23	N

Notes.
[a] Photometric measurement.
[b] Marginal detection.
[c] Indicates whether this object met the updated selection criteria described in Section 3.

Among the 46 LAE candidates from Becker et al. (2018) targeted for spectroscopic follow-up, 14 were also selected as LAEs in this work using the updated PSF photometry and the new LAE selection criteria. Of those 14, 11 were spectroscopically confirmed at $\geqslant 4\sigma$ confidence, and one was marginally detected at 1.4σ. Figure 9 shows the 1D spectra for these PSF-selected LAEs. The dashed cyan lines indicate skyline residuals, and the dotted pink line indicates the flux-weighted mean wavelength of the emission line.

The remaining 32 objects targeted for spectroscopic follow-up were selected as LAEs only by Becker et al. (2018). Of these, seven are spectroscopically confirmed LAEs, and their 1D spectra are shown in Figure 10. These seven fell just outside of our new selection criteria using the updated PSF photometry; four had narrow band $4.5 < S/N < 5$, and one had $S/N = 3.2$. The remaining two are detected in the $r2$ band at 2.3σ, which is slightly higher than our $r2$ cuts allow. The other 25 objects failed our updated selection criteria by wider margins. Their spectroscopic non-detections are attributed to the issues with CModel fluxes described in Section 3.1, with the exception of one object, which was a low-redshift contaminant displaying a clear [O III] emission line.

In summary, we find a high spectroscopic confirmation rate (11 plus one marginal detection out of 14) among candidates selected using our updated photometry and selection criteria. The two non-detected objects of the photometrically-selected group were generally fainter than their detected counterparts, with a 1σ upper limit on their flux being consistent with the photometric measurement, and showed no sign of being low-redshift contaminants. We note that all of the objects followed up spectroscopically were also selected as LAEs by Becker et al. (2018), so these 14 candidates do not represent an unbiased random sample from the new photometric catalog. Nevertheless, the high confirmation rate among the PSF-selected candidates gives us confidence that the photometric selection methods described in Section 3.2 should yield a high-fidelity sample of LAEs.

Appendix C
Comparison to Becker 2018 LAE Catalog

Here we compare the LAE catalog presented in this work, using updated photometry and selection criteria as described in Sections 3.2 and 3.1, to that published in Becker et al. (2018).

In this work, we identify 641 LAE candidates in the J0148 field, compared to 806 LAEs presented in Becker et al. (2018). Of the objects selected by Becker et al. (2018), 398 had NB816 < 25.5 as required in this work, and 236 of those objects ($\sim$60%) are selected using the selection criteria and photometric measurements outlined in Section 3. We estimate that 15%–20% of the objects selected by Becker et al. (2018) with NB816 < 25.5 were affected by the systematic CModel flux effects described in Section 3. We show examples of objects wrongly rejected and accepted due to these issues in Figure 11. Each cutout image is $10''$ on each side and centered on the object position. The wrongly rejected object was rejected based on artificially high broadband fluxes, while the wrongly accepted object had inflated NB816 flux. The remaining 20%–25% of the Becker et al. (2018) objects with NB816 < 25.5 missing from our sample are within 1σ errors of meeting our selection criteria. Given that our catalog is $\sim$50% complete at the faintest magnitudes, it is not unexpected that some objects will not be selected due to photometric scattering.

Table 6 summarizes the number of LAEs selected in both catalogs. Because the two catalogs use different narrowband magnitude limits, NB816 $\leqslant$ 25.5 in this work and NB816 $\leqslant$ 26.0 in Becker et al. (2018), we provide the number of objects selected in each catalog using both limits. We emphasize that this work only makes use of NB816 $\leqslant$ 25.5 objects for our analysis; the fainter magnitude limit is provided only for comparison. Table 6 also summarizes the number of LAEs that are common to both catalogs using both magnitude limits, as well as the number of objects common to the catalogs as is (using NB816 $\leqslant$ 25.5 for the objects selected in this work and NB816 $\leqslant$ 26.0 for Becker et al. (2018), as published).
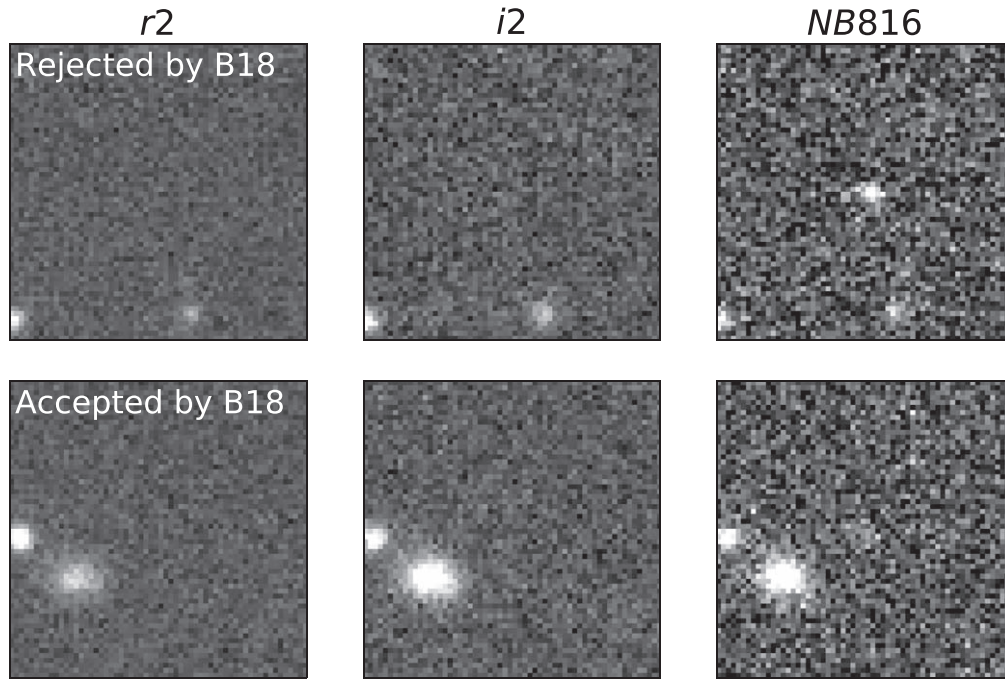
Figure 11. Examples of objects rejected (top row) and accepted (bottom row) as LAE candidates by Becker et al. (2018) based on spurious CModel photometry. Each cutout is $10''$ on each side and centered on the object position. The rejected object is detected in the CModel photometry at 10σ in the narrow band, 18σ in $i2$, and 26σ in $r2$—a clear case of artificially high broadband photometry. This object is selected as an LAE in this work using the photometry and selection criteria outlined in Section 3. The accepted object is undetected in the broad bands, but is detected using the CModel photometry at 7.5σ in the narrow band, compared to 3.0σ using our PSF photometry.

Table 6
Comparison of LAE Selections in Becker et al. (2018) and This Work

	This Work	Becker et al. (2018)
Objects selected with NB816 $\leqslant$ 26.0	784[a]	806
Objects selected with NB816 $\leqslant$ 25.5	641	398[b]
		Both Works
Catalog overlap with NB816 $\leqslant$ 26.0[c]		366
Catalog overlap with NB816 $\leqslant$ 25.5[d]		236
Catalog overlap with published NB816 limits[e]		321

Notes.
[a] This work uses a brighter magnitude limit than Becker et al. (2018) (NB816 $\leqslant$ 25.5). The number of objects selected with the fainter limit is included only for comparison.
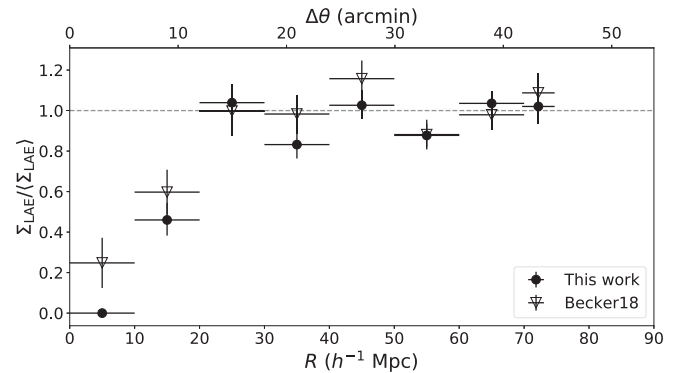[b] Likewise, Becker et al. (2018) use NB816 $\leqslant$ 26.0. The subset of this catalog that satisfies the brighter magnitude limit is included here for comparison.
[c] The number of LAEs appearing in both catalogs that meet the fainter magnitude requirement, NB816 $\leqslant$ 26.0 (as in Becker et al. 2018).
[d] The number of LAEs appearing in both catalogs that meet the brighter magnitude requirement, NB816 $\leqslant$ 25.5 (as in this work).
[e] The number of LAEs appearing in both catalogs as is, using NB816 $\leqslant$ 25.5 for this work and NB816 $\leqslant$ 26.0 for Becker et al. (2018; as published).

Figure 12. Surface density of completeness-corrected LAEs in the J0148 field, as selected in this work (filled circles) and by Becker et al. (2018; open triangles). The surface density is measured in annuli of width 10 h^{-1} Mpc for all except the outermost bin, which has a width of 4.5 h^{-1} Mpc. All surface densities are normalized by the mean value in the respective work, calculated over $15' \leqslant \theta \leqslant 40'$. The horizontal error bars show the width of the annuli, and the vertical error bars are 68% Poisson intervals.

Figure 7 shows the distribution of LAE candidates in the J0148 field, as presented in this work (left) and in Becker et al. (2018; center). Each LAE is color-coded according to the NB816 magnitude in its respective catalog. This work has a shallower narrowband magnitude limit than Becker et al. (2018); therefore, we have shown LAEs that fall in the $25.5 \leqslant$ NB816 $\leqslant 26.0$ bin from the Becker et al. (2018) catalog with black crosses, as they are fainter than our selection criteria

allow. The quasar (yellow star) is centered in each panel, and the dotted, concentric circles show increments of 10 h^{-1} Mpc. The solid outer circle marks the edge of the field of view, $45'$ from the quasar. The LAE candidates are shown plotted over a surface density map, which we create by kernel density estimation over a regular grid of $0'.24$ pixels using a Gaussian kernel of bandwidth $0'.15$. The surface density map is normalized by the mean surface density of the field. While the exact membership is varied between the two catalogs, both catalogs show similar large-scale structures.

Figure 12 shows the surface density as a function of radial distance from the quasar in the J0148 field, as measured here (circles) and by Becker et al. (2018; triangles). The surface densities

are measured in 10 h^{-1} Mpc annuli for all except the outermost bin, which is 4.5 h^{-1} Mpc, and normalized by the mean surface density, which is measured over $15' \leqslant \theta \leqslant 40'$. We note that, in addition to the changes to fluxing and LAE selection criteria, the completeness corrections used in this work (see Section 4) are different than those used by Becker et al. (2018). However, in most radial bins, the surface density measurements are consistent within the 1σ errors.

To summarize, the results in the J0148 field are largely unchanged between this work and Becker et al. (2018). Approximately 50% of the LAEs selected in this work are also selected by Becker et al. (2018), and outside of the photometry issues described in Section 3.1, the variations are as expected given that each catalog is ~50% complete in its faintest magnitude bin. The two catalogs trace similar large-scale structures (see Figure 7), most notably both

displaying the ~20 h^{-1} Mpc void in the center of the field, along the quasar line of sight.

Appendix D
Completeness Corrections

Figure 13 shows the completeness measured in both fields as a function of distance from the quasar and NB816 magnitude. We determine the completeness by injecting a catalog of artificial LAE candidates across each field and then applying the LAE selection criteria described in Section 3. We bin the artificial LAEs by magnitude and distance from the quasar. The completeness is then computed as the fraction of artificial LAEs detected in each bin. The observations are binned in the same way and corrected by the reciprocal of the completeness in each bin.
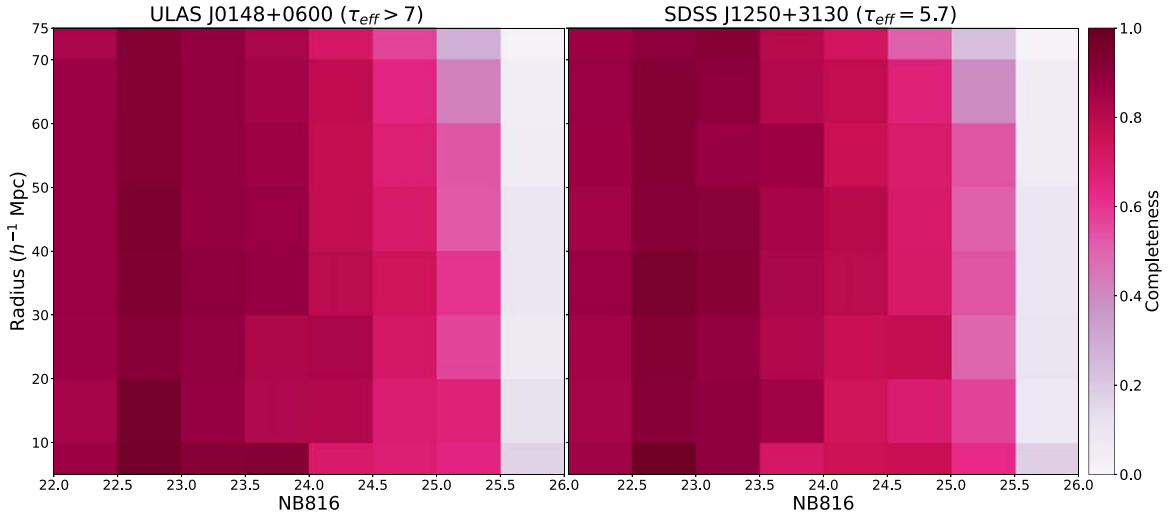
Figure 13. Completeness measured in the J0148 field (left) and J1250 field (right) as a function of NB816 magnitude and distance to the quasar. The completeness is based on the detection rate of artificial LAEs injected in each field, and is given by the fraction of artificial LAEs detected in each radius and magnitude bin.

ORCID iDs

Holly M. Christenson ⬤ https://orcid.org/0000-0002-0421-065X
George D. Becker ⬤ https://orcid.org/0000-0003-2344-263X
Steven R. Furlanetto ⬤ https://orcid.org/0000-0002-0658-1243
Frederick B. Davies ⬤ https://orcid.org/0000-0003-0821-3644
Matthew A. Malkan ⬤ https://orcid.org/0000-0001-6919-1237
Yongda Zhu ⬤ https://orcid.org/0000-0003-3307-7525

References

Abazajian, K., Adelman-McCarthy, J. K., Agüeros, M. A., et al. 2004, AJ, 128, 502
Astropy Collaboration, Robitaille, T. P., Tollerud, E. J., et al. 2013, A&A, 558, A33
Bañados, E., Venemans, B. P., Mazzucchelli, C., et al. 2018, Natur, 553, 473
Becker, G. D., Bolton, J. S., Madau, P., et al. 2015, MNRAS, 447, 3402
Becker, G. D., Davies, F. B., Furlanetto, S. R., et al. 2018, ApJ, 863, 92
Bertin, E., & Arnouts, S. 1996, A&AS, 117, 393
Bosch, J., Armstrong, R., Bickerton, S., et al. 2018, PASJ, 70, S5
Bosman, S. E. I., Davies, F. B., Becker, G. D., et al. 2021, arXiv:2108.03699
Bosman, S. E. I., Fan, X., Jiang, L., et al. 2018, MNRAS, 479, 1055
Bouwens, R. J., Illingworth, G. D., Oesch, P. A., et al. 2015, ApJ, 803, 34
Chambers, K. C., Magnier, E. A., Metcalfe, N., et al. 2016, arXiv:1612.05560
Chardin, J., Haehnelt, M. G., Aubert, D., & Puchwein, E. 2015, MNRAS, 453, 2943
Chardin, J., Puchwein, E., & Haehnelt, M. G. 2017, MNRAS, 465, 3429
Choudhury, T. R., Paranjape, A., & Bosman, S. E. I. 2021, MNRAS, 501, 5782
D'Aloisio, A., McQuinn, M., Davies, F. B., & Furlanetto, S. R. 2018, MNRAS, 473, 560
D'Aloisio, A., McQuinn, M., & Trac, H. 2015, ApJL, 813, L38
D'Aloisio, A., Upton Sanderbeck, P. R., McQuinn, M., Trac, H., & Shapiro, P. R. 2017, MNRAS, 468, 4691
Davies, F. B., Becker, G. D., & Furlanetto, S. R. 2018a, ApJ, 860, 155
Davies, F. B., & Furlanetto, S. R. 2016, MNRAS, 460, 1328
Davies, F. B., Hennawi, J. F., Bañados, E., et al. 2018b, ApJ, 864, 142
Díaz, C. G., Koyama, Y., Ryan-Weber, E. V., et al. 2014, MNRAS, 442, 946
Dijkstra, M., & Wyithe, J. S. B. 2012, MNRAS, 419, 3181
Eilers, A.-C., Davies, F. B., & Hennawi, J. F. 2018, ApJ, 864, 53
Faber, S. M., Phillips, A. C., Kibrick, R. I., et al. 2003, Proc. SPIE, 4841, 1657
Fan, X., Strauss, M. A., Becker, R. H., et al. 2006, AJ, 132, 117
Gangolli, N., D'Aloisio, A., Nasir, F., & Zheng, Z. 2021, MNRAS, 501, 5294
Garaldi, E., Compostella, M., & Porciani, C. 2019, MNRAS, 483, 5301
Greig, B., Mesinger, A., & Bañados, E. 2019, MNRAS, 484, 5094
Greig, B., Mesinger, A., Haiman, Z., & Simcoe, R. A. 2017, MNRAS, 466, 4239
Hunter, J. D. 2007, CSE, 9, 90
Ivezić, Ž., Kahn, S. M., Tyson, J. A., et al. 2019, ApJ, 873, 111
Jung, I., Finkelstein, S. L., Dickinson, M., et al. 2020, ApJ, 904, 144
Jurić, M., Kantor, J., Lim, K., et al. 2015, arXiv:1512.07914
Kashino, D., Lilly, S. J., Shibuya, T., Ouchi, M., & Kashikawa, N. 2020, ApJ, 888, 6
Keating, L. C., Kulkarni, G., Haehnelt, M. G., Chardin, J., & Aubert, D. 2020a, MNRAS, 497, 906
Keating, L. C., Weinberger, L. H., Kulkarni, G., et al. 2020b, MNRAS, 491, 1736
Kelson, D. D. 2003, PASP, 115, 688
Khostovan, A. A., Sobral, D., Mobasher, B., et al. 2019, MNRAS, 489, 555
Konno, A., Ouchi, M., Shibuya, T., et al. 2017, PASJ, 70, S16
Kulkarni, G., Keating, L. C., Haehnelt, M. G., et al. 2019a, MNRAS, 485, L24
Kulkarni, G., Worseck, G., & Hennawi, J. F. 2019b, MNRAS, 488, 1035
Lidz, A., Oh, S. P., & Furlanetto, S. R. 2006, ApJL, 639, L47
Mason, C. A., Treu, T., Dijkstra, M., et al. 2018, ApJ, 856, 2
McGreer, I. D., Fan, X., Jiang, L., & Cai, Z. 2018, AJ, 155, 131
McGreer, I. D., Mesinger, A., & D'Odorico, V. 2015, MNRAS, 447, 499
McGreer, I. D., Mesinger, A., & Fan, X. 2011, MNRAS, 415, 3237
Morales, A., Mason, C., Bruton, S., et al. 2021, ApJ, 919, 120
Mortlock, D. J., Warren, S. J., Venemans, B. P., et al. 2011, Natur, 474, 616
Nasir, F., & D'Aloisio, A. 2020, MNRAS, 494, 3080
Ouchi, M., Harikane, Y., Shibuya, T., et al. 2018, PASJ, 70, S13
Ouchi, M., Shimasaku, K., Akiyama, M., et al. 2008, ApJS, 176, 301
Parsa, S., Dunlop, J. S., & McLure, R. J. 2018, MNRAS, 474, 2904
Planck Collaboration, Aghanim, N., Akrami, Y., et al. 2020, A&A, 641, A6
Price-Whelan, A. M., Sipőcz, B. M., Günther, H. M., et al. 2018, AJ, 156, 123
Qin, Y., Mesinger, A., Bosman, S. E. I., & Viel, M. 2021, MNRAS, 506, 2390
Shibuya, T., Ouchi, M., Konno, A., et al. 2018, PASJ, 70, S14
Stark, D. P., Ellis, R. S., Chiu, K., Ouchi, M., & Bunker, A. 2010, MNRAS, 408, 1628
Trac, H., Cen, R., & Mansfield, P. 2015, ApJ, 813, 54
Tramonte, D., Rubiño-Martín, J. A., Betancort-Rijo, J., & Dalla Vecchia, C. 2017, MNRAS, 467, 3424
Trapp, A. C., & Furlanetto, S. R. 2020, MNRAS, 499, 2401
van der Walt, S., Colbert, S. C., & Varoquaux, G. 2011, CSE, 13, 22
Virtanen, P., Gommers, R., Oliphant, T. E., et al. 2020, NatMe, 17, 261
Wang, F., Davies, F. B., Yang, J., et al. 2020, ApJ, 896, 23
Wise, J. H. 2019, ConPh, 60, 145
Yang, J., Wang, F., Fan, X., et al. 2020, ApJ, 904, 26
Zhu, Y., Becker, G. D., & Bosman, S. E. I. 2021, arXiv:2109.06295